

Measuring the Real Point Spread Function of High Numerical Aperture Microscope Objective Lenses

Rimas Juškaitis

INTRODUCTION

Testing and characterization of high-quality lenses have been perfected into fine art with the advent of lasers, phase-shifting interferometers, charge-coupled device (CCD) cameras, and computers. A bewildering array of techniques is described in Malacara's classic reference book on the subject (Malacara, 1992). Several of these techniques, in particular the Twyman–Green interferometer and the star test, are applicable to testing of microscope objective lenses.

Characterizing high numerical aperture (NA) objective lenses presents unique challenges. Many of the standard approaches, including Twyman–Green interferometry, are in fact comparative techniques. They require a reference object — an objective or a concave reflective surface — of the same or larger numerical aperture and of perfect (comparatively speaking) optical quality. This is problematic. Even if two lenses of the same type are available, a problem still remains of apportioning the measured aberrations to the individual lenses. The star test, which is absolute, hits a similar problem in that the Airy disk produced by the lens being tested is impossible to observe directly, and hence it has to be magnified by a lens with a similar or better resolution, that is, higher NA. Immersion lenses create further complications. All tests described in this chapter are free from these problems. They are absolute and use a small point scatterer or a flat mirror to create a reference wavefront against which the lens aberrations are checked. Together with advanced interferometric techniques and processing algorithms, this results in a range of techniques suitable for routine characterization of all available microscope objective lenses.

A few words have to be said regarding identity of the lenses used throughout this chapter. Although the principal data for the specimens used in our test is given, the name of their manufacturers is not. This is done for several reasons, not least to avoid accusations of not using most up-to-date lenses from company A to make it look worse than company B. As a university laboratory we rely on the stock of lenses which have accumulated over the years. A few people also brought their own lenses to test. Not all of these are necessarily the best in class. This work is about testing techniques and typical problems with high NA lenses, not about relative merits of individual lenses or their respective manufacturers.

Before describing specific lens testing techniques it might be useful to repeat here a few basic facts about microscope objective lenses in general. Modern objective lenses are invariably designed for infinite conjugate ratio, that is, the object of observation is placed in the front focal plane and its image is formed at infinity. In order to obtain a real intermediate image, a separate lens, called

the tube lens, is used. The focal length of this lens F (which ranges from 165 mm for Zeiss and 180 mm for Olympus to 200 mm for Leica and Nikon) together with the magnification of the objective M gives the focal length of the objective $f = F/M$.

One of the basic postulates of aberration-free lens design is that it has to obey Abbe's sine condition. For a microscope objective treated as a thick lens, this can be interpreted as the fact that its front principal surface is actually a sphere of radius f centered at the front focus. Any ray leaving the focus at an angle α to the optical axis is intercepted by this surface at the height $d = f \sin \alpha$ and emerges from the back-focal plane parallel to the axis at the same height, as shown in Figure 11.1. For immersion lenses this has to be multiplied by the refractive index of the immersion fluid n .

In most high NA objective lenses, the back-focal plane, also called the pupil plane, is located inside the lens and is not, therefore, physically accessible. Fortunately, lens designers tend to put an aperture stop as close to this plane as possible, which greatly simplifies the task of identifying the pupil plane when re-imaging it using an auxiliary lens. Any extra elements, such as phase rings in phase contrast lenses or variable aperture iris diaphragms, will also be located in the back-focal plane.

The physical aperture of an objective lens D is related to its numerical aperture $n \sin \alpha$ via

$$D = \frac{2Fn \sin \alpha}{M}. \quad (1)$$

Ultimately it is limited by the size of the objective thread. For a modern low magnification high NA immersion lens with, say, $n \sin \alpha = 1$ and $M = 20$, D can be as large as 20 mm. This is one of the reasons why some lens manufacturers (notably Leica and Nikon) have now abandoned the former gold standard of the Royal Microscopical Society (RMS) thread and moved to larger thread sizes.

Every infinity-corrected lens needs a field lens to produce the intermediate image. Field lenses differ considerably between manufacturers and even between their various microscope ranges. Strictly speaking, one should test each objective lens together with its matching tube lens. We chose not to do this for several reasons. First, there is general movement to confine all aberration correction to the objective lens. The only aberration that is still sometimes corrected in the tube lens is the lateral color. This does not affect the results of our measurements. Moreover, there is a tendency to use objective lenses individually without their respective field lenses, especially in laboratory-built scanning systems. All this implies the importance of knowing imaging properties of high NA objective lenses as individual units.

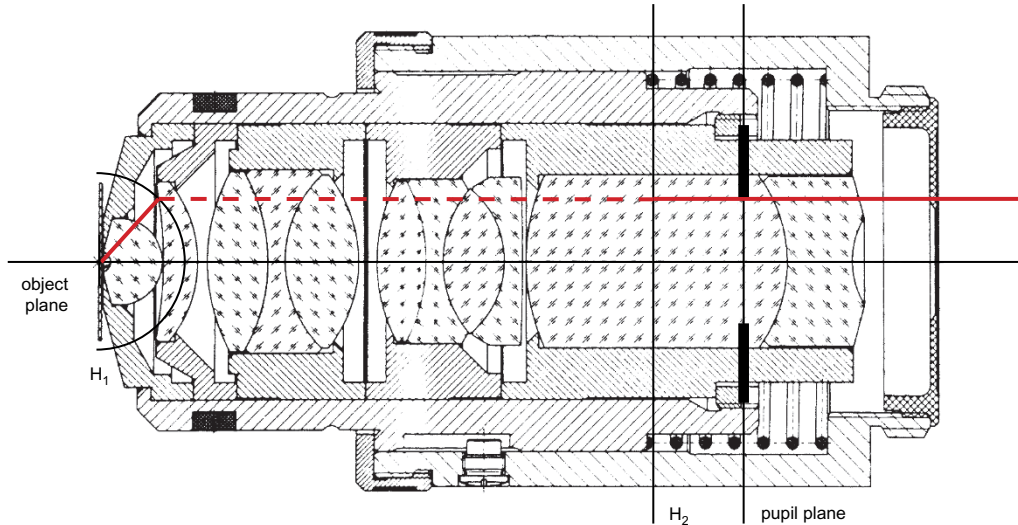


FIGURE 11.1. Schematic diagram of a typical high NA planapochromat objective lens. Principal surfaces, aperture stop, and marginal ray are indicated.

MEASURING POINT SPREAD FUNCTION

A perfect lens transforms a plane wave front into a converging spherical wave. If they are not too dramatic, any deviations from this ideal behavior can be described by introducing a complex Pupil Function $P(\rho, \theta)$, where ρ is the normalized radial coordinate in the pupil plane and μ is the azimuthal angle in the same plane. Both amplitude and phase aberrations can be present in a lens, but it is the latter that usually play the dominant role. The amplitude aberrations are typically limited to some apodization towards the edge of the pupil; these are discussed in more detail in the section “Apodization.”

The optical field distribution produced by this (possibly aberrated) converging wave is termed the point spread function, or PSF, of the lens. This distribution can be obtained in its most elegant form if dimensionless optical coordinates in lateral

$$v = \frac{2\pi}{\lambda} n \sin \alpha \sqrt{x^2 + y^2} \quad (2)$$

and axial

$$u = \frac{8\pi}{\lambda} n \sin^2 \frac{\alpha}{2} z \quad (3)$$

directions are used. In these coordinates the intensity distribution in the PSF is independent of the NA of the lens, and the surface $u = v$ corresponds to the edge of the geometric shadow. The actual focal field distribution in these newly defined cylindrical coordinates is given by (Born and Wolf, 1998):

$$h(u, v, \psi) = A \exp \left[\frac{i u}{4 \sin^2 \frac{\alpha}{2}} \right] \int_0^1 \int_0^{2\pi} P(\rho, \theta) \times \exp \left\{ -i \left[v \rho \cos(\theta - \psi) + \frac{u \rho^2}{2} \right] \right\} \rho d\rho d\theta. \quad (4)$$

The exponential term in front of the integral is nothing else than a standard phase factor of a plane wave $2\pi n z / \lambda$.

For the aberration-free case $P = 1$ and the integral over θ can be calculated analytically to give $2\pi J_0(v\rho)$. Equation 4 now simplifies to

$$h(u, v) = 2\pi A \exp \left[\frac{i u}{4 \sin^2 \frac{\alpha}{2}} \right] \int_0^1 \exp \left(-\frac{i u \rho^2}{2} \right) J_0(v\rho) \rho d\rho. \quad (5)$$

This equation is readily calculated either numerically or using Lommel functions. The resulting intensity distributions are well known and can be found, for example, in Born and Wolf (1998). Not only that, but also PSFs subjected to various aberrations have been calculated countless times in the past and are instantly recognizable to most microscopists. It is precisely for this reason that a relatively straightforward measurement of the PSF can frequently provide an instant indication of what is wrong with a particular objective lens.

Equations 4 and 5 are, of course, scalar approximations. This approximation works remarkably well up to angular apertures of about 60° . Even above these angles the scalar approximation can be safely used as a qualitative tool. For those few lenses that seem to be beyond the scalar approach (and for the rigorous purists) there is always an option to use a well-developed vectorial theory (Richards and Wolf, 1959).

Fiber-Optic Interferometer

The requirement to measure both amplitude and phase of the PSF calls for an interferometer-based setup. The fiber-optic interferometer, Figure 11.2, that was eventually chosen for the task has several important advantages. It is an almost common-path system, which dramatically improves long-term stability. It is also a self-aligning system: light coupled from the fiber to the lens and scattered in the focal region is coupled back into the fiber with the same efficiency. For convenience, the whole setup is built around a single-mode fiber-optic beam-splitter, the second output of which is index-matched in order to remove the unwanted reflection. A helium–neon (He–Ne) laser operating at 633 nm is used as a light source. The whole setup bears cunning resemblance to a confocal microscope. In fact, it is a confocal microscope, or at least can be used as such (Wilson *et al.*, 1994). Provided that light emerging from the fiber overfills the pupil of the objective lens, the former acts as an effective pinhole ensuring spatial filtering of the backscattered light (see Chapter 26, *this volume*). Thus, if the

object can be regarded as a point scatterer, then the amplitude of the optical signal captured by the fiber

$$R \sim h^2 = |h|^2 \exp[2i \arg(h)] \quad (6)$$

that is, its magnitude is equal to the intensity of the PSF whereas the phase is twice the phase of the PSF. In order to measure both these parameters, light reflected back along the fiber from the tip is used as a reference beam r . Wavefronts of both signal and reference beams are perfectly matched in a single-mode fiber — this is the beauty of the fiber-optic interferometer. Furthermore, the fiber tip is dithered to introduce a time-varying phase shift between the interfering beams $\phi(t) = \phi_0 \cos \omega t$. The interference signal reaching the photodetector is now given by

$$I = |r + R|^2 = r^2 + |R|^2 + 2r[\operatorname{Re}(R)\cos(\phi_0 \cos \omega t) - \operatorname{Im}(R)\cos(\phi_0 \cos \omega t)], \quad (7)$$

where r was assumed to be real for simplicity. It is now a simple matter to extract both $\operatorname{Re}(R)$ and $\operatorname{Im}(R)$ from this signal by using lock-in detection technique. The signal of Eq. 7 is multiplied by $\cos \omega t$ and the result is low-pass filtered to give

$$I_1 = rJ_1(\phi_0)\operatorname{Im}(R), \quad (8)$$

whereas synchronous demodulation with $\cos 2\omega t$ yields

$$I_2 = rJ_0(\phi_0)\operatorname{Re}(R). \quad (9)$$

By appropriately adjusting the modulation amplitude ϕ_0 , it is easy to achieve $J_1(\phi_0) = J_2(\phi_0)$ and, by substituting Eq. 6, to calculate

$$h \sim \sqrt{I_1^2 + I_2^2} \exp\left(\frac{i}{2} \arctan \frac{I_1}{I_2}\right). \quad (10)$$

Thus, the goal of obtaining both the amplitude and phase of the PSF of the objective lens has been achieved. Of course, in order to obtain full two- (2D) or three-dimensional (3D) PSF corresponding scanning of the object, the point scatterer is still required.

Point Spread Function Measurements

In order to demonstrate the effectiveness of this method in detecting small amounts of aberrations, it was tested on a special kind of objective lens. This 60×1.2 NA water-immersion plan-

apochromat was developed for deconvolution applications and hence was specifically designed to have a well-corrected PSF. It was also equipped with a correction collar to compensate for cover glass thicknesses in the range 0.14 to 0.21 mm. One hundred nanometer colloidal gold beads mounted beneath a #1.5 coverslip of nominal thickness (0.17 mm) acted as point scatterers in this case. The coverslip was in turn mounted on a microscope slide and a gap between them was filled with immersion oil so as to eliminate reflection from the back surface of the coverslip. The size of the bead was carefully chosen experimentally in order to maximize the signal level without compromising the point-like behavior. Indeed, a control experiment using 40 nm beads yielded similar results to those presented below but with a vastly inferior signal-to-noise ratio.

In principle, this apparatus is capable of producing full 3D complex PSF data sets. It was found however that in most cases xz -cross-sections provided sufficient insight into the aberration properties of the lens without requiring too long acquisition times. Such results are shown in Figure 11.3 for two settings of the correction collar. In order to emphasize the side lobe structure, the magnitude of the PSF is displayed in decibels with the peak value taken to be 0 dB. It can be seen that a collar setting of 0.165 mm gives a near-perfect form to the PSF. The axial side lobes are symmetric with respect to the focal plane and the phase fronts away from this plane quickly assume the expected spherical shape. On the other hand, a small 10% deviation from the correct setting already has a quite pronounced effect on the PSF in the bottom row of Figure 11.3. The symmetry is broken, the axial extent of the PSF has increased by about 30%, and distinct phase singularities appeared on the phase fronts. Everything points towards a certain amount of uncompensated spherical aberration being present in the system. It is interesting to note that, as the phase map of the PSF seems to be more sensitive to the aberrations than the magnitude, this can be used as an early warning indicator of the trouble. It also underlines the importance of measuring both the magnitude and phase of the PSF.

Although so far the measured PSF has been described in purely qualitative terms, some useful quantitative information about the objective lens can also be extracted from these data. One parameter that can be readily verified is the objective's NA. Axial extent of the PSF is more sensitive to the NA than its lateral shape. Using

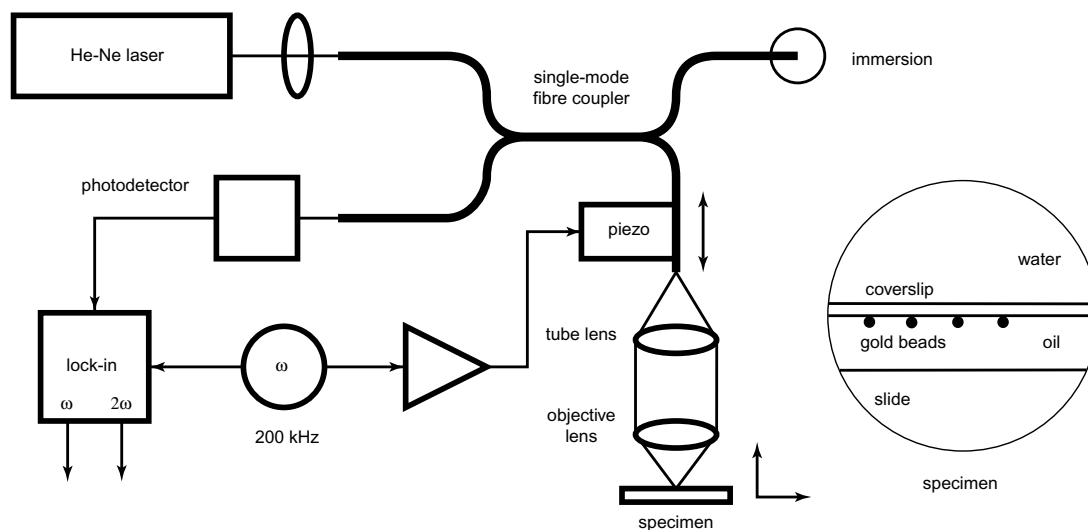


FIGURE 11.2. Schematic diagram of the fiber-optic interferometer-based setup for measuring objective PSFs.

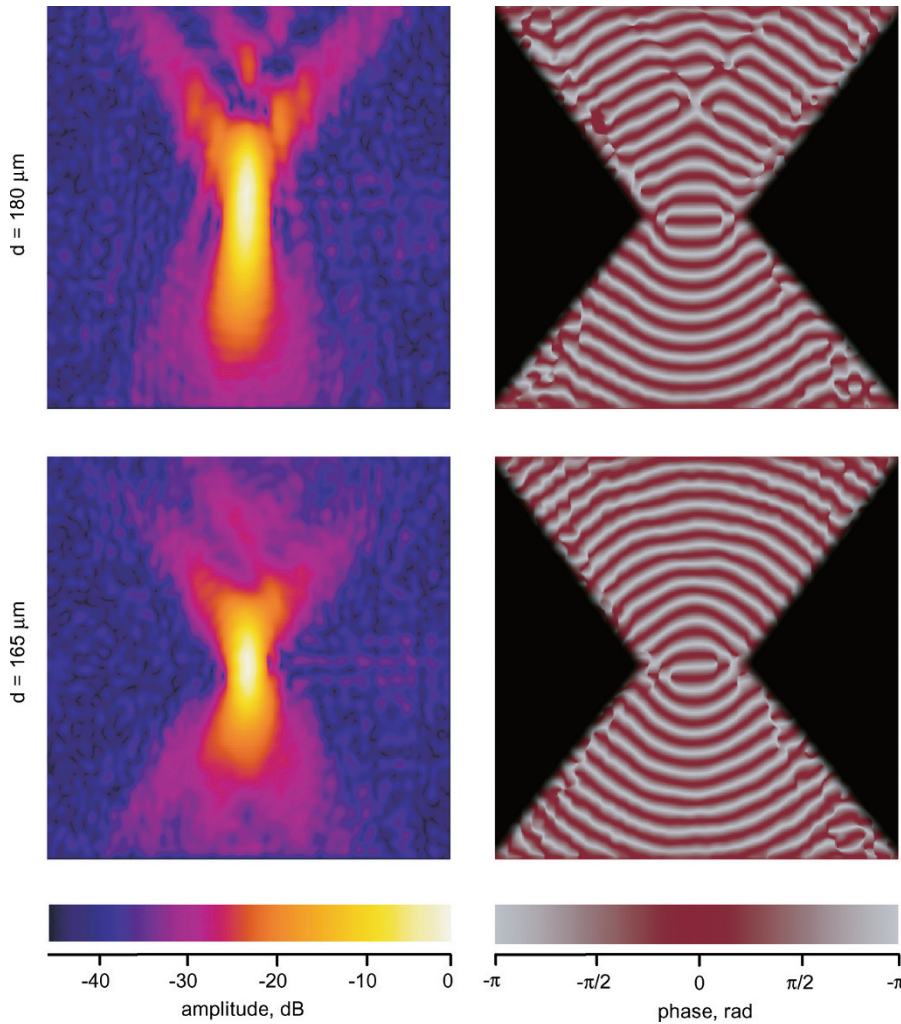


FIGURE 11.3. The amplitude and phase of the effective PSF for 60×1.2 NA water-immersion lens with correction collar. Results for two different collar settings are shown. Image size in both x (horizontal) and z (vertical) are $5 \mu\text{m}$.

the axial section of the PSF is therefore the preferred method to determine the NA. Besides, the interference fringes present in the z -scan provide a natural calibration scale for the distance in z . The actual measurement was obtained by finding the best fit to the curve in Figure 11.4. A somewhat surprising result of this exercise

was that the best fit corresponded to NA of 1.15, rather than the nominal value of 1.2. This is not a coincidence: such discrepancies were found with other high NA objective lenses as well. The reason for this kind of behavior will become clear in the section “Pupil Function.”

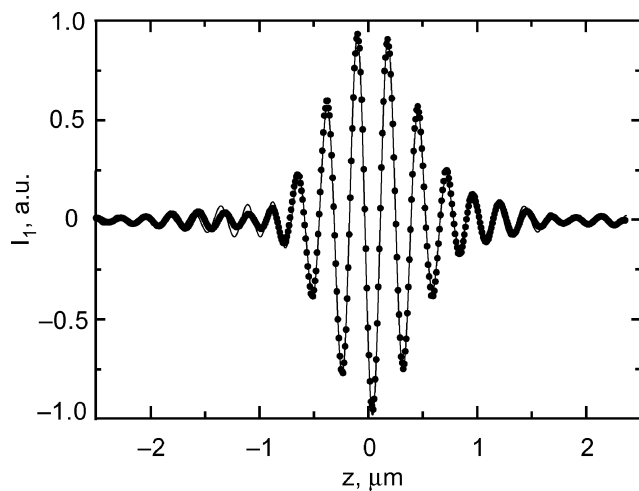


FIGURE 11.4. Measured (*dots*) and calculated (*line*) amplitude axial responses for the same lens.

CHROMATIC ABERRATIONS

Chromatic aberrations constitute another class of aberrations that can adversely affect the performance of any microscopy system. These aberrations are notoriously difficult to overcome in high NA objective lens design. The reason, at least in part, is the relative uniformity of dispersion properties of common glasses used in objective lenses. Ingenious solutions have been found at an expense of dramatic increase of the number of lens elements — typically to more than a dozen in apochromats. Even then, part of the correction may need to be carried out in the elements external to the objective.

Lateral and axial color, as they are called by lens designers, are usually treated as separate chromatic aberrations. The former, which manifests itself as the wavelength-dependent magnification, is easy to spot in conventional microscopes as coloring of the edges of high-contrast objects. Lateral chromatic aberration is also the more difficult of the two to correct. Traditionally this has been done by using the tube lens, or even the ocular, to offset the residual lateral color of the lens. Some of the latest designs claim

to have achieved full compensation within the objective lens itself — claims to be treated with caution. The correct testing procedure for the lateral color should include at least a matched tube lens. The simplest test would probably be to repeat the experiments described in the section “PSF Measurements” for several wavelengths at the edge of the field of view and record the shift of the lateral position of the point image.

In confocal microscopy, where the signal is determined by the overlap of the effective excitation and detection PSFs, the loss of register between them should lead to a reduction of signal towards the edge of the field of view. It has to be said, though, that in most confocal microscopes, almost always, only a small area around the optical axis is used for imaging, hence this apodization is hardly ever appreciable. Axial color, on the other hand, is rarely an issue in conventional microscopy, but it can be of serious consequence for confocal microscopy, especially when large wavelength shifts are involved, such as in multi-photon or second and third harmonic microscopy. Mismatch in axial positions of excitation and detection PSFs can easily lead to degradation or even complete loss of signal, even in the center of the field of view. Below we describe a test setup which uses this sensitivity of the confocal system to characterize axial chromatic aberration of high NA objective lenses.

Apparatus

Ideally, one could conceive an apparatus similar to that in Figure 11.2, whereby the laser is substituted with a broadband light source. One problem is immediately obvious: it is very difficult to couple any significant amount of power into a single-mode fiber from a broadband light source, such as an arc lamp. Using multiple lasers provides only a partial (and expensive) solution. Instead, it was decided to substitute the point scatterer with a plane reflector. Scanning the reflector axially produces the confocal signal (Wilson and Sheppard, 1984):

$$I = \left[\frac{\sin u/2}{u/2} \right]^2. \quad (11)$$

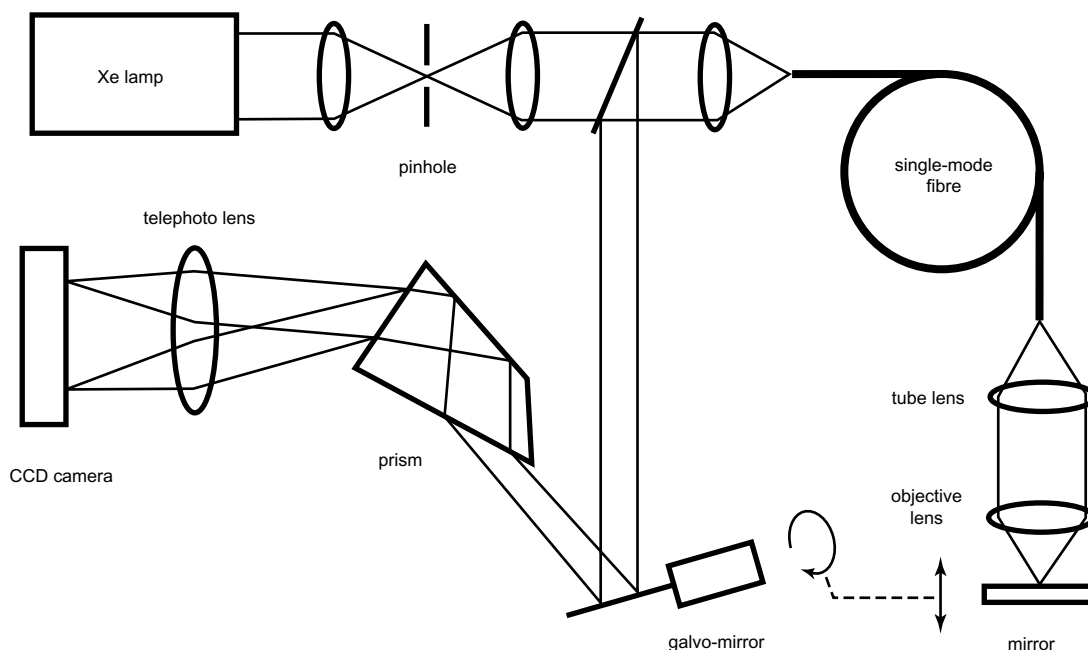


FIGURE 11.5. Experimental setup for measuring axial chromatic aberration of objective lenses.

The maximum signal is detected when the plane reflector lies in the focal plane. This will change with the wavelength if chromatic aberration is present. Using a mirror instead of a bead has another advantage: the resulting signal is one-dimensional, function of u only, and hence a dispersive element can be used to directly obtain 2D spectral axial responses without the necessity of acquiring multiple datasets at different wavelengths.

The resulting apparatus, depicted in Figure 11.5 and described in more detail in Juškaitis and Wilson (1999), is again based around a fiber-optic confocal microscope setup, but the interferometer part is now discarded. Instead, a monochromator prism made of SF4 glass is introduced to provide the spectral spread in the horizontal direction (i.e., in the image plane). Scanning in the vertical direction was introduced by a galvo-mirror moving in synchronism with the mirror in the focal region of the objective lens. The resulting 2D information is captured by a cooled 16-bit slow-scan CCD camera. A small-arc Xe lamp is used as a light source providing approximately $0.2 \mu\text{W}$ of broadband visible radiation in a single-mode fiber. This is sufficient to produce a spectral snapshot of a lens in about 10 s.

Axial Shift

Typical results obtained by the chromatic aberration measurement apparatus are shown in Figure 11.6. Because the raw images are not necessarily linear either in z or λ , a form of calibration procedure in both coordinates is required. To achieve this, the arc lamp light source was temporarily replaced by a He-Ne and a multi-line Ar⁺ lasers. This gave enough laser lines to perform linearization in λ . As a bonus, coherent laser radiation also gave rise to interference fringes in the axial response with the reflection from the fiber tip acting as a reference beam, just as in the setup shown in Figure 11.2. When a usual high NA objective lens was substituted with a low NA version, these fringes covered the whole range of the z -scan and could be readily used to calibrate the axial coordinate. The traces shown in Figure 11.6 have been normalized to unity at each individual wavelength. The presence of longitudinal chromatic aberration is clearly seen in both plots. Their shapes are

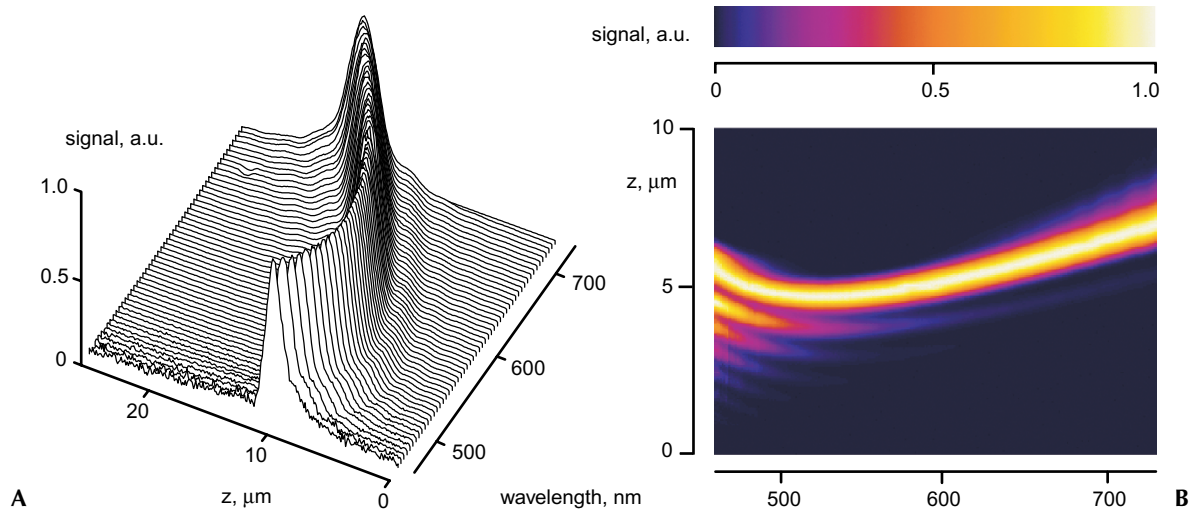


FIGURE 11.6. Experimental results from (A) 32×0.5 NA plan-achromat objective, displayed as 3D plot, and (B) 50×0.8 NA plan-achromat in pseudo-color representation. Note the change in z -scale.

characteristic for achromats in which the longitudinal color is corrected for two wavelengths only. It is interesting also to note the change of the shape of the axial response with the wavelength. This is noticeable for a 32×0.5 NA plan-achromat but it becomes particularly dramatic for a 50×0.8 NA plan-achromat [Fig. 11.6(b)]. Clearly the latter lens suffers from severe spherical aberration at wavelengths below 550 nm, which results in multiple secondary maxima at one side of the main peak of the axial response.

An interesting problem is posed by the tube lens in Figure 11.5. This lens may well contribute to the longitudinal chromatic aberration of the microscope as a whole and, therefore, it is desirable to use here a proper microscope tube lens matched to the objective. In fact it transpired that in some cases the tube lens exhibited significantly larger axial color aberration than the objective itself. This is hardly surprising: a typical tube lens is a simple triplet and, sometimes, even a singlet. Clearly, it is impossible to achieve any sophisticated color correction in such an element taken separately, therefore the objective lens would have to be designed to take this imperfection into account. Further information on this can be found in Chapter 7.

In this experiment, however, the main task was to evaluate the properties of the objective lens itself. A different approach was therefore adopted. The same achromatic doublet (Melles Griot 01 LAO 079) collimating lens was used with all objective lenses. Because the chromatic aberrations of this lens are well documented in the company literature, these effects could be easily removed from the final results presented in Figure 11.7. Figure 11.7(B) presents the same data but in a form more suited to confocal microscopy, whereby the chromatic shift is now expressed in optical units as defined in Eq. 3. The half width of the axial response to a plane mirror is then given by 2.78 optical units at all wavelengths and for all NAs. This region is also shown in the figure. The zero in the axial shift is arbitrarily set to correspond to $\lambda = 546$ nm for all the objectives tested.

As could be expected these results show improvement in performance of apochromats over achromats. They also show that none of the tested objectives (and this includes many more not shown in Figure 11.7 for fear of congestion) could meet the requirement of having a spectrally flat — to within the depth of field — axial behavior over the entire visible range. This was only

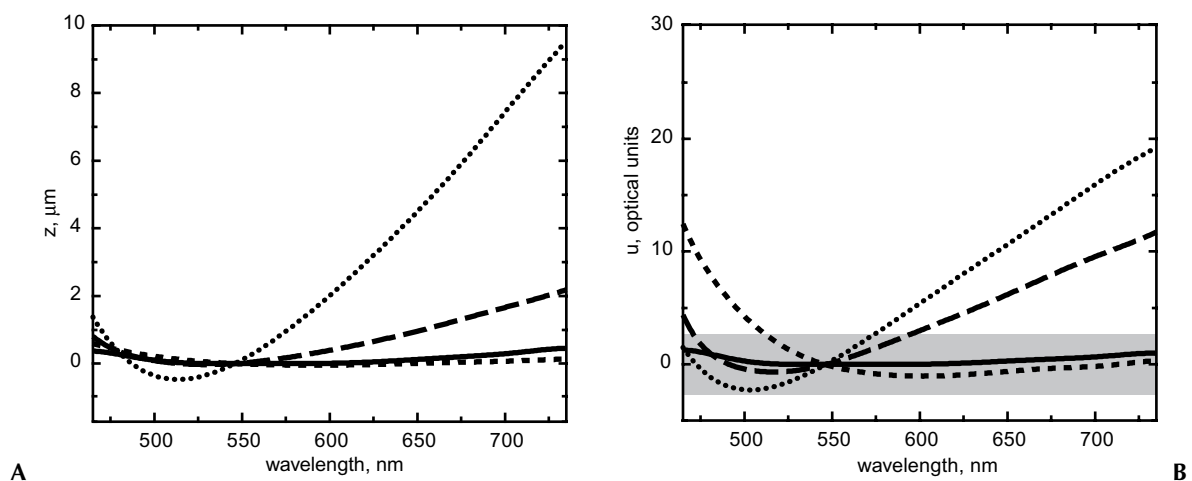


FIGURE 11.7. Wavelength dependence of the axial response maxima represented in physical (A) and optical (B) axial coordinates. The four traces correspond to: 32×0.5 NA plan-achromat (*dotted line*), 50×0.8 NA plan-achromat (*long dashes*), 100×1.4 NA plan-apochromat (*short dashes*), and the same lens stopped down to 0.7 NA (*solid line*).

possible to achieve by stopping down a 1.4 NA apochromat using a built-in aperture stop — the trick to be repeated several times again before this chapter expires.

PUPIL FUNCTION

Pupil function is the distribution of the phase and amplitude across the pupil plane when the lens is illuminated by a perfect spherical wave from the object side. It is related in scalar approximation to the PSF via a Fourier-like relationship (Eq. 4). It would appear, therefore, that they both carry the same information and therefore the choice between them should be a simple matter of convenience. Reality is a bit more complicated than that. Calculating the pupil function from the PSF is an ill-posed problem and therefore very sensitive to noise. Measurements of the pupil function provide direct and quantitative information about the aberrations of the lens — information that can only be inferred from the PSF measurements.

The trouble with mapping the pupil function is that a source of a perfect spherical wave is required. Such a thing does not exist but, fortunately, the dipole radiation approximates such a wave rather well, at least as far as phase is concerned. The approach described in this section is based on using small side-illuminated scatterers as sources of spherical waves. The actual pupil function measurement is then performed in a phase-shifting Mach-Zehnder interferometer in a rather traditional fashion.

Phase-Shifting Interferometry

The experimental setup depicted in Figure 11.8 comprised a frequency doubled Nd:YAG laser which illuminated a collection of 20 nm diameter gold beads deposited on the surface of a high refractive index glass prism acting as dipole scatterers (Juškaitis *et al.*, 1999). Because the laser light suffers total internal reflection at the surface of the prism, no direct illumination can enter the objective lens. The gold scatterers convert the evanescent field into the radiating spherical waves that were collected by the lens and converted into plane waves. These waves were then superimposed on a collimated reference wave. A 4-f lens system was then used to image the pupil plane of the lens onto a CCD camera. A pinhole in the middle of this projection system served to select a signal from a single scatterer. The size of this pinhole had to be carefully controlled so as not to introduce artifacts and degrade resolution in the image of the pupil function. A second CCD camera was employed to measure the PSF at the same time.

One of the mirrors in the reference arm of the interferometer was mounted on a piezoelectric drive and moved in synchronism with the CCD frame rate to produce successive interferograms of the pupil plane shifted by $2\pi/3$ rad

$$I_l \sim \left| r + P(\rho, \theta) \exp\left(i \frac{2\pi l}{3}\right) \right|^2, \quad l = 0, 1, 2. \quad (12)$$

Using these three measurements the phase component of the pupil function was then calculated as

$$\arg[P(\rho, \theta)] = \arctan \frac{\sqrt{3}(I_1 - I_2)}{I_1 + I_2 - 2I_0}. \quad (13)$$

The lens, together with the prism, was mounted on a pivoting stage which could rotate the whole assembly around the axis aligned to an approximate location of the pupil plane. Thus, the off-axis as well as on-axis measurements of the pupil function could be obtained. A set of such measurements is presented in Figure 11.9, which clearly demonstrates how the performance of the lens degrades towards the edge of the field of view. Not only appreciable astigmatism and coma are introduced, but also vignetting becomes apparent. The presence of vignetting would be very difficult to deduce from direct measurements of the PSFs shown in Figure 11.10, as it could be easily mistaken for astigmatism. Not that such vignetting is necessarily an indication that something is wrong with the lens; it may well be deliberately introduced there by the lens designer to block off the most aberrated part of the pupil.

Zernike Polynomial Fit

Traditionally, the phase aberrations of the pupil functions are described quantitatively by expanding them using a Zernike circle polynomial set:

$$\arg[P(\rho, \theta)] = \sum_{i=1}^{\infty} a_i Z_i(\rho, \theta), \quad (14)$$

where a_i are aberration coefficients for corresponding Zernike polynomials $Z_i(\rho, \theta)$. Significant variations between different modifications of Zernike polynomials exist. In this work a set from Mahajan (1994) was used. The first 22 members of this set are listed in Table 11.1 together with their common names. This list can be further extended. In practice, however, expansion beyond the second-order spherical aberration is not very reliable due to experimental errors and noise in the measured image of $P(\rho, \theta)$.

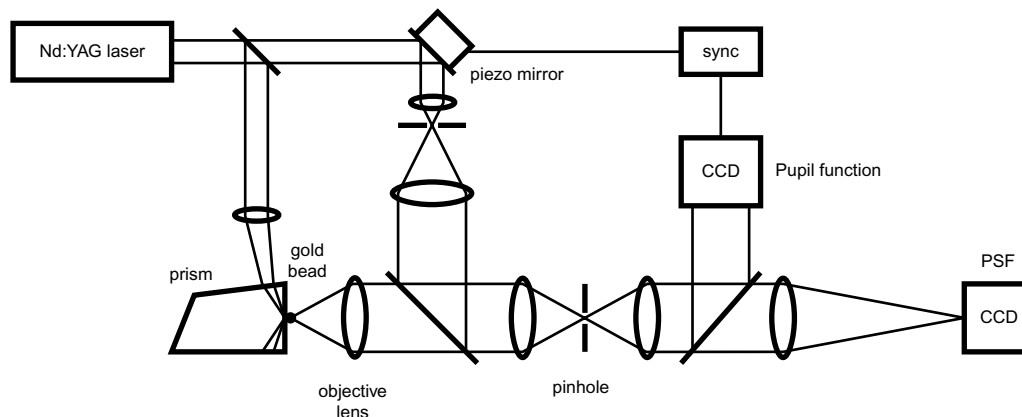


FIGURE 11.8. Phase-shifting Mach-Zehnder interferometer used for the pupil function measurements. Laser is frequency-doubled Nd:YAG laser.

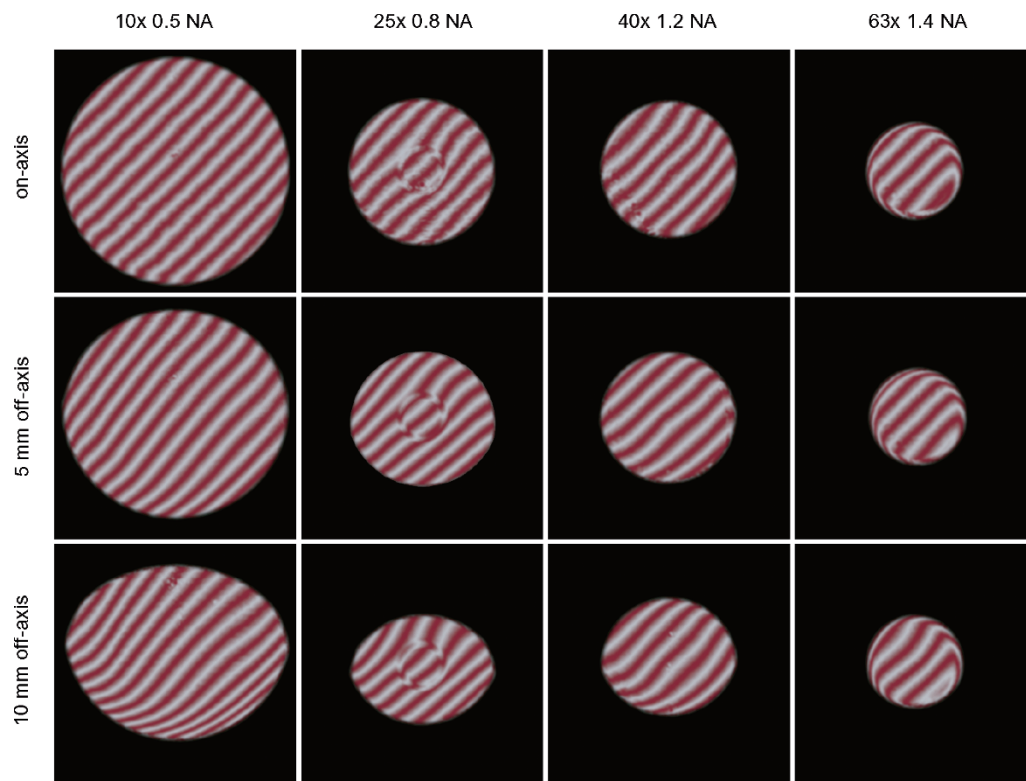


FIGURE 11.9. Phase distributions in the pupil plane of a representative range of objective lenses. Left to right: 10 × 0.5 NA, 25 × 0.8 NA multi-immersion, 40 × 1.2 NA water-immersion, and 63 × 1.4 NA oil-immersion objectives. Performance at the different positions in the field of view as measured in the intermediate image plane is shown. Regular phase tilt added to facilitate visualization.

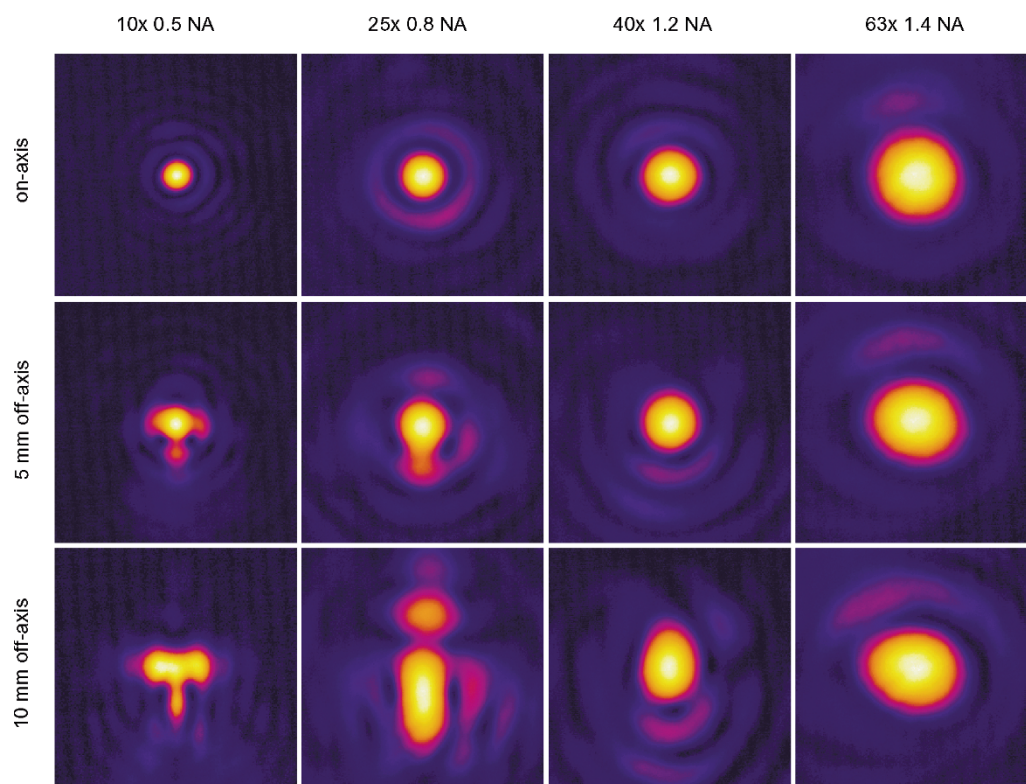


FIGURE 11.10. Point spread functions for the same lenses as in Figure 11.9.

TABLE 11.1. Orthonormal Zernike Circle Polynomials

i	n	m	$Z_i(r, \theta)$	Aberration Term
1	1	0	1	Piston
2	1	1	$2r \cos \theta$	Tilt
3	1	-1	$2r \sin \theta$	Tilt
4	2	0	$\sqrt{3}(2r^2 - 1)$	Defocus
5	2	2	$\sqrt{6}r^2 \cos 2\theta$	Astigmatism
6	2	-2	$\sqrt{6}r^2 \sin 2\theta$	Astigmatism
7	3	1	$2\sqrt{2}(3r^3 - 2r) \cos \theta$	Coma
8	3	-1	$2\sqrt{2}(3r^3 - 2r) \sin \theta$	Coma
9	3	3	$2\sqrt{2}r^3 \cos 3\theta$	Trefoil
10	3	-3	$2\sqrt{2}r^3 \sin 3\theta$	Trefoil
11	4	0	$\sqrt{5}(6r^4 - 6r^2 + 1)$	Primary spherical
12	4	2	$\sqrt{10}(4r^4 - 3r^2) \cos 2\theta$	
13	4	-2	$\sqrt{10}(4r^4 - 3r^2) \sin 2\theta$	
14	4	4	$\sqrt{10}r^4 \cos 4\theta$	
15	4	-4	$\sqrt{10}r^4 \sin 4\theta$	
16	5	1	$2\sqrt{3}(10r^5 - 12r^3 + 3r) \cos \theta$	
17	5	-1	$2\sqrt{3}(10r^5 - 12r^3 + 3r) \sin \theta$	
18	5	3	$2\sqrt{3}(5r^5 - 4r^3) \cos 3\theta$	
19	5	-3	$2\sqrt{3}(5r^5 - 4r^3) \sin 3\theta$	
20	5	5	$2\sqrt{3}r^5 \cos 5\theta$	
21	5	-5	$2\sqrt{3}r^5 \sin 5\theta$	
22	6	0	$\sqrt{7}(20r^6 - 30r^4 + 12r^2 - 1)$	Secondary spherical

The determination of the expansion coefficients a_i should, in principle, be a simple procedure, given that the Zernike polynomials are orthonormal. Multiplying the measured pupil function by a selected polynomial and integrating over the whole pupil area should directly yield the corresponding aberration coefficient. The real life is a bit more complicated, especially when processing the off-axis data, such as shown in Figure 11.9. One obstacle is vignetting: the standard Zernike set is no longer orthonormal over a non-circular pupil. Even without vignetting, the 2π phase ambiguity poses a problem. Before the expansion procedure can be applied, the phase of the pupil function has to be unwrapped — not necessarily a trivial procedure.

An entirely different expansion technique was developed to overcome these difficulties. This technique is based on a simulated, iterative wavefront correction routine, originally conceived to be used in adaptive optics applications together with a diffractive optics wavefront sensor (Neil *et al.*, 2000). The essence of the method is that small simulated amounts of individual Zernike aberrations are applied in turns to the measured pupil function. After each variation, the in-focus PSF is calculated and the whole process iteratively repeated until the Strehl ratio is maximized. The final magnitudes of the Zernike terms are then taken to be (with opposite signs) the values of the Zernike expansion coefficients of the experimentally measured, aberrated pupil function. This procedure is reasonably fast and sufficiently robust, provided that the initial circular aperture can still be restored from the vignetted pupil.

The power of this technique is demonstrated in Figure 11.11, where a 40×1.2 NA water-immersion lens was investigated at three different settings of the correction collar. As expected, adjusting the collar mainly changes the primary and secondary spherical aberration terms. Variations in the other terms are negligible. The optimum compensation is achieved close to $d = 0.15$ mm setting, where small amounts of both aberrations with opposite signs cancel each other. The usefulness of the Zernike expansion is further demonstrated by the fact that the main residual term in

this case was the defocus, which, although not an aberration itself, could be easily mistaken for a spherical aberration upon visual inspection of the interference pattern.

Restoration of a 3D Point Spread Function

Nowhere is the power of the pupil function approach to the objective lens characterization more apparent than in cases when the full 3D shape of the PSF needs to be determined. Such need may arise, for example, when using deconvolution techniques to process images obtained with a confocal microscope.

As is clear from Eq. 4, it is not only possible to calculate an in-focus PSF from a measured pupil function, but the same can be done for any amount of defocus by choosing an appropriate value for the axial coordinate u . Repeating the process at regular steps in u yields a set of through-focus slices of the PSF. These can then be used to construct a 3D image of the PSF in much the same manner that 3D images are obtained in a confocal microscope. Compared to the direct measurement using a point scatterer, advantages of this approach are clear. A single measurement of the pupil function is sufficient and no scanning of the bead in three dimensions is required. Consequently, exposures per image pixel can be much longer. As a result, this method provides much improved signal-to-noise ratio in the final rendering of the PSF, allowing even the faintest sidelobes to be examined.

Obviously, presenting a complete 3D image on a flat page is always going to be a problem but, as Figure 11.12 shows, even just two meridional cross-sections of a 3D PSF provide infinitely more information than a plain 2D in-focus section of the same PSF at the bottom of Figure 11.9. Thus, for example, the yz -section clearly shows that the dominant aberration for this particular off-axis position is coma. Comparing the two sections it is also possible to note different convergence angles for the wavefronts in two directions — a direct consequence of vignetting.

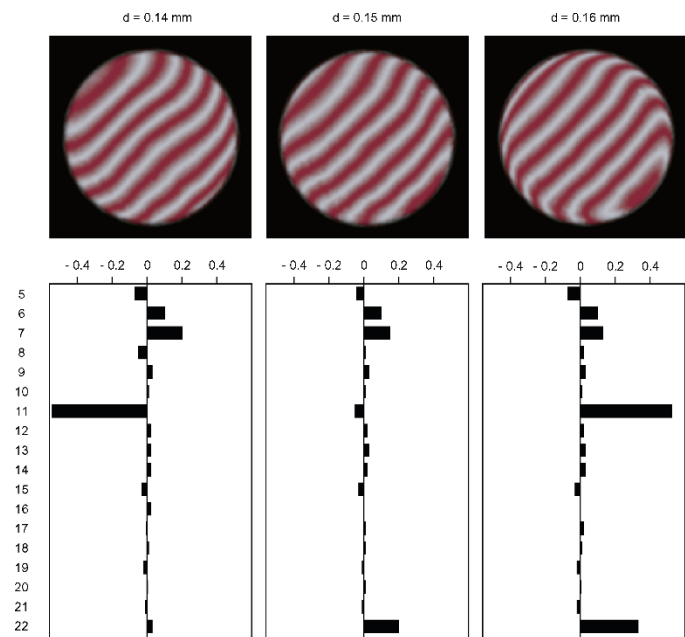


FIGURE 11.11. Variations in wavefront aberration function expressed via Zernike modes when correction collar of a water-immersion lens is adjusted.

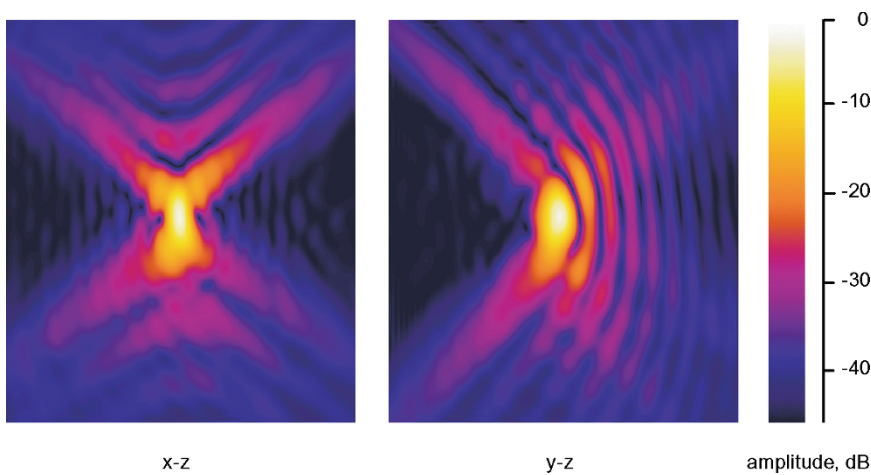


FIGURE 11.12. Three-dimensional PSF restored from pupil function data, shown here via two meridional sections.

Empty Aperture

Testing objective lenses with highest NAs (1.4 for oil, 1.2 for water immersion), one peculiar aberration pattern is often encountered. As shown in Figure 11.13, the lens is well corrected up to 90% to 95% of the aperture radius, but after that we see a runaway phase variation right to the edge. Speaking in Zernike terms, residual spherical aberration components of very high order are observed. Because of this high order, it appears unlikely that the aberrations are caused by improper immersion fluid or some other trivial reason. These would manifest themselves via low-order spherical as well. More realistically, this is a design flaw of the lens.

The portion of the lens affected by this feature varies from few to about 10%. For the lens in Figure 11.13, the line delimiting the effective aperture was somewhat arbitrarily drawn at NA = 1.3. What is undeniable is that the effect is not negligible. In all likelihood, this form of aberration is the reason for the somewhat mysterious phenomenon when a high NA lens exhibits a PSF that is perfect in all respects except for an apparently reduced NA. This was the case in “PSF Measurements” and also described by other researchers (Hell *et al.*, 1995).

It is quite clear that competitive pressures push the lens designers towards the boundary (and sometimes beyond the boundary) of the technical possibilities of the day. A few years ago no microscope lens manufacturer could be seen without a 1.4 NA oil-immersion lens when the Joneses next door were making one. The

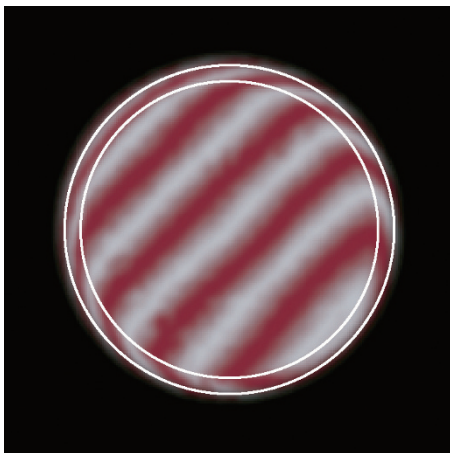


FIGURE 11.13. Pupil function of 63 × 1.4 NA oil immersion lens with both nominal (outer ring) and effective working (inner ring) apertures indicated.

plot is likely to be repeated with the newly emerging 1.45 NA lenses. It is also true that a hefty premium is charged by the manufacturers for the last few tenths in the NA. It is quite possible that in many cases this is a very expensive *empty* aperture, which, although physically present, does not contribute to the resolving power of the lens.

This discussion may seem to be slightly off the point because many users buy high NA lenses not because of their ultimate resolution, but because of their light gathering efficiency in fluorescence microscopy. This property is approximately proportional to NA^2 and therefore high NA lenses produce much brighter, higher contrast images. At first glance it may seem that the aberrated edge of the pupil will not affect this efficiency and hence buying a high NA lens, however aberrated, still makes sense. Unfortunately, this is not true. Because the phase variation at the edge is so rapid, the photons passing through it reach the image plane very far from the optical axis. They do not contribute to the main peak of the diffraction spot, instead they form distant sidelobes. In terms of real life images, it means that the brightness of the background, and not the image itself, is increased. Paradoxically, blocking the outermost portion of the pupil would in this case *improve* the image contrast!

The last statement may well be generalized in the following way: in the end, the only sure way of obtaining a near-perfect high NA objective lens is to acquire one with larger-than-required nominal NA and then stop it down. Incidentally, in certain situations this may be happening even without our deliberate intervention. Consider using an oil immersion lens on a water-based sample: no light at $NA > 1.33$ can penetrate the sample anyway and hence the outer aperture of the lens is effectively blocked. Not that such use should be ever considered unless in dire need: see Chapter 20 for a graphic description of the Bad Things that will happen.

MISCELLANEA

In this section a few more results obtained with the pupil function evaluation apparatus are presented. These need not necessarily be of prime concern to most microscope users but might be of interest to connoisseurs and, indeed, could provide further insight into how modern objective lenses work.

Temperature Variations

Many microscopists should recall seeing 23°C on a bottle of immersion oil as a temperature at which the refractive index is

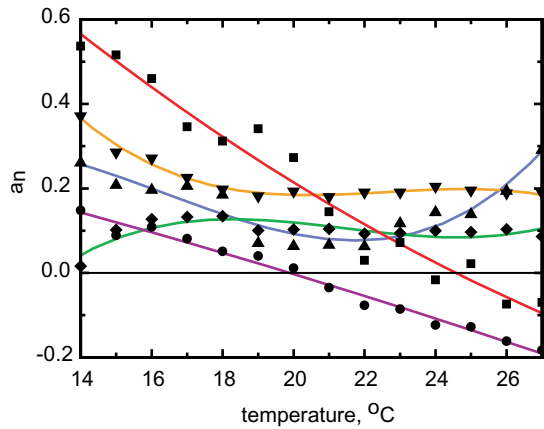


FIGURE 11.14. Temperature variation of primary (red) and secondary (purple) spherical aberrations as well as magnitudes of astigmatism (blue), coma (orange), and trefoil (green). The latter three were defined as $a = \sqrt{a_s^2 + a_c^2}$, where a_s^2 and a_c^2 are the sine and cosine components of the corresponding aberrations.

specified, typically $n = 1.518$ at $\lambda = 546$ nm. But how important is this standard laboratory temperature to the performance of high NA lenses? In order to answer this question, the pupil function of a 100×1.4 NA oil-immersion lens was measured at a range of temperatures and the results were processed to obtain the variation of the primary aberration coefficients with the temperature.

The major factor in the degradation of the imaging qualities of the immersion lenses with temperature is the variation of the refractive index of the immersion oil, usually at the level of $dn/dT = 3 - 4 \times 10^{-4}$. The effect of this change is similar to that of introducing a layer of a refractive-index-mismatched material between the lens and the sample. The resulting aberrations are well understood, their exhaustive analysis can be found in Török and colleagues (1995). In short, spherical aberrations of various orders will be generated; the relative weight of higher-order terms rises dramatically with the NA of the lens. This is corroborated by the experimental data in Figure 11.14 which show steady, almost linear variation in both the primary and secondary spherical aberration terms with temperature. Less predictably, the same plot also registers significant variations in the other first-order aberrations: coma, astigmatism, and trefoil. Because of their asymmetry, these aberrations cannot be explained by the oil refractive index changes. They are probably caused by small irregular movements of individual elements within the objective lens itself.

Strictly speaking, aberrations caused by refractive index changes in the immersion fluid should not be regarded as lens aberrations. In practice, however, the lenses are designed for a particular set of layers of well-defined thicknesses and refractive indexes between the front of the lens and the specimen. Any change in these parameters upsets the fine optical phase balance in the system and results in aberrated PSF. This might be an argument why it makes sense to treat the immersion medium as being a part of the objective lens. The temperature effect depends dramatically on the type of the immersion fluid used. Water with $dn/dT \approx 8 \times 10^{-5}$ is far less sensitive; dry lenses, of course, are not affected at all. Long-working-distance lenses will be at a disadvantage too due to longer optical paths in the immersion fluid.

Closer analysis of Figure 11.14 reveals that the aberrations are indeed minimized around 23°C , where the combined primary and secondary spherical aberrations are close to their minimum. A small but noticeable hysteresis effect was also noted when, after a few temperature cycles, the aberration coefficients failed to return to their low initial values. It is tempting to connect this effect to the fact that the imaging properties of even the best of lenses always deteriorate with age — although accidental straining during experiments is still likely to remain the prevailing factor.

Polarization Effects

Polarization effects encountered when imaging a dipole with a high NA lens have been covered elsewhere (Wilson *et al.*, 1997). For the purposes of this investigation they are interesting inasmuch as the imperfections of the lens contribute to them. When an image of a small scatterer is viewed between the crossed polarizers, a characteristic “clover leaf” pattern emerges. An image of the pupil plane, Figure 11.15, is particularly telling. It shows that only the rays that travel very close to the edge of the pupil pass through the polarizer.

This happens because the polarization of light in these four segments is slightly rotated from its original x -direction. The reason for this rotation is 2-fold. First of all the radiation of a dipole is linearly polarized in the meridional plane, which can only be approximated by a uniformly polarized plane wave for small angles α . When this spherical wavefront is straightened by the lens and projected into the pupil plane, only light propagating in xz and yz possesses perfect x -polarization, the remainder is rotated to some degree. The degree of rotation increases dramatically with higher aperture angles. This effect is fundamentally geometrical; its close cousin is a well-known problem of how to comb a hairy ball.

The second reason for the polarization rotation is more prosaic: Fresnel losses. These tend to be higher for s than for p polarized

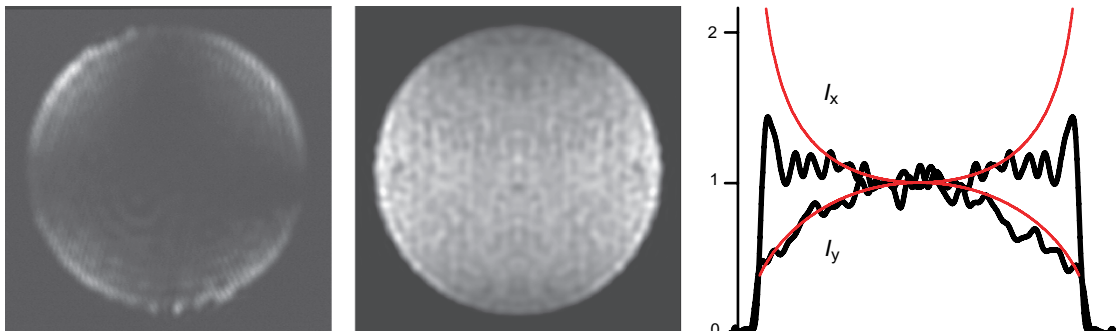


FIGURE 11.15. Polarization and apodization effects in a high NA lens. An image of a dipole scatterer viewed at the pupil plane of a 100×1.4 NA lens with crossed (left) and parallel (center) analyzers. Principal cross-sections, together with the theoretical predictions according to Eq. 15 (red line), are also shown.

light. For a beam travelling in a plane bisecting the xz - and yz -planes, the overall tendency would be to rotate the polarization towards the radial direction. Hence, this effect seems to work in the opposite direction to that caused by the geometric factor, which favors the azimuthal direction.

Apodization

So far the emphasis of this investigation has been on measuring the phase aberrations. This is justified by the fact that the phase deviations from an ideal spherical wavefront have considerably more impact on the shape of the PSF than similar imperfections in amplitude. Nevertheless, for completeness' sake it might be interesting now to have a closer look at the apodization effects occurring in high NA lenses. Using dipole radiation as a probe offers unique advantages in this task. Because the angular intensity distribution of the dipole radiation is well defined, any deviations from perfect lens behavior should be easy to spot.

Let's assume that the polarization vector of a dipole situated in the focus is aligned in the x -direction. Angular intensity distributions in the xz - and yz - (i.e., meridional and equatorial) planes will be given by, respectively, $I_x \sim \cos^2 \alpha$ and $I_y = \text{const}$. Due to purely geometric reasons, these distributions will change when light propagates to the pupil plane even if the lens is perfect. With reference to Figure 11.11 and to the sine condition $d = nf \sin \alpha$, it is not too difficult to show that an extra factor of $\sec \alpha$ has to be introduced when going from the object to the pupil side of the objective in order to satisfy the energy conservation law. This factor has been well known since the early days of high NA lens theory (Richards and Wolf, 1959). Intensity distributions in the pupil plane should therefore look like $I_x \sim \cos \alpha$ and $I_y \sim \sec \alpha$ or, with the help of sine condition:

$$I_x \sim \frac{nf}{\sqrt{(nf)^2 - d^2}}, \quad I_y \sim \frac{\sqrt{(nf)^2 - d^2}}{nf}. \quad (15)$$

An experiment to measure these distributions was carried out on the setup shown in Figure 11.8 by simply blocking the reference beam and capturing the pupil intensity image alone. To produce the results shown in Figure 11.15 images of eight individual scatterers were acquired and averaged in the computer. Intensity distributions in the two principal planes were then extracted. They follow the theoretical predictions rather well up to about half of the pupil radius. After that, apodization is apparent, and increases gradually, reaching about 30% to 50% towards the edge of the pupil.

The cause of this apodization in all likelihood is the Fresnel losses in the elements of the objective lens. Broadband anti-reflection coatings applied to these elements are less effective at the higher incidence angles that the high aperture rays are certain to encounter. Because of the nature of these losses, they are likely to be very individual for each particular type of objective lens. It is also worth noting a slight polarization dependence of the losses that contributes to polarization effects described in the previous section.

CONCLUSION

The range of experimental setups and techniques dedicated to the characterization of the high NA objective lenses could be continued. For example, the lateral chromatic aberration has not been considered thus far. One has to be practical, however, and draw a line at some point.

From the tests described in this chapter, the measurement of the pupil function provides the most detailed and insightful information about the capabilities of a particular lens. In many cases, two or three pupil functions measured across the field of view and, perhaps, tabulated in the form of Zernike coefficients, would be more than sufficient to predict the lens performance in most practical situations. It is disheartening to think of how much wasted time, frustration, and misunderstandings could be avoided if such information were to be supplied with the objective lenses by their manufacturers.

My overall conclusion is that the vast majority of currently designed objective lenses perform really well. Any imperfections visible in a microscope image are far more likely to be a result of a sloppy practice (e.g., tilted coverslip, incorrect immersion fluid, etc.) than of a fault of the lens itself. That said, cutting-edge designs are always going to be a problem and the very highest NA lenses should be approached with caution. It is also worth pointing out that elements of the microscope other than the objective lens may also be a factor in imaging quality. The tube lens is one such element of particular concern. Having evolved little over the last years, this lens simply has too few elements to achieve the aberration correction on par with that of an all-singing all-dancing objective lens. This situation is further exacerbated by the advent of a new breed of low magnification high NA objectives with their enormous back apertures.

ACKNOWLEDGMENT

I thank my colleagues M.A.A. Neil and T. Wilson for numerous contributions to this work.

REFERENCES

- Born, M., and Wolf, M., 1998, *Principles of Optics*, Pergamon Press, Oxford.
- Hell, S.W., Hanninen, P.E., Kuusisto, A., Schrader, M., and Soini, E., 1995, Annular aperture 2-photon excitation microscopy, *Opt. Commun.* 117:20–24.
- Juškaitis, R., and Wilson, T., 1998, The measurement of the amplitude spread function of microscope objective lens, *J. Microsc.* 189:8–11.
- Juškaitis, R., and Wilson, T., 1999, A method for characterizing longitudinal chromatic aberration of microscope objectives using a confocal optical system, *J. Microsc.* 195:17–22.
- Juškaitis, R., Neil, M.A.A., and Wilson, T., 1999, Characterizing high quality microscope objectives: a new approach, *SPIE Proc.* 3605:140–145.
- Mahajan, V.N., 1994, Zernike circle polynomials and optical aberrations of systems with circular pupils, *Appl. Optics* 33:8121–8124.
- Malacara, D., 1992, *Optical Shop Testing*, John Wiley and Sons, New York.
- Neil, M.A.A., Booth, M.J., and Wilson, T., 2000, New modal wave-front sensor: A theoretical analysis, *J. Opt. Soc. Am. A* 17:1098–1107.
- Richards, B., and Wolf, E., 1959, Electromagnetic diffraction in optical systems II. Structure of the image field in an aplanatic system, *Proc. Roy. Soc. Lond. A* 253:358–379.
- Török, P., Varga, P., and Németh, G., 1995, Analytical solution of the diffraction integrals and interpretation of wave-front distortion when light is focused through a planar interface between materials of mismatched refractive-indexes, *J. Opt. Soc. Am. A* 12:2660–2671.
- Wilson, T., and Sheppard, C.J.R., 1984, *Theory and Practice of Scanning Optical Microscopy*, Academic Press, London.
- Wilson, T., Juškaitis, R., Rea, N.P., and Hamilton, D.K., 1994, Fibre optic confocal and interference microscopy, *Opt. Commun.* 110:1–6.
- Wilson, T., Juškaitis, R., and Higdon, P.D., 1997, The imaging of dielectric point scatterers in confocal and conventional polarisation microscopes, *Opt. Commun.* 141:298–313.